

On the origin of graben and ridges within and near volcanically buried craters and basins in Mercury's northern plains

Andrew M. Freed,¹ David M. Blair,¹ Thomas R. Watters,² Christian Klimczak,³ Paul K. Byrne,³ Sean C. Solomon,^{3,4} Maria T. Zuber,⁵ and H. J. Melosh¹

Received 7 May 2012; revised 4 September 2012; accepted 5 September 2012; published 17 October 2012.

[1] Images of Mercury's northern volcanic plains taken by the MESSENGER spacecraft reveal a large number of buried impact craters and basins discernible by wrinkle-ridge rings that overlie their rims. Many of these "ghost" craters and basins contain interior graben of diverse widths and orientations. Here we use finite element models to test a variety of mechanisms for the formation of these graben and ridges. Results show that graben are best explained by cooling of large thicknesses of flood lavas within the craters and basins; conservation of surface area during cooling induces the required extensional stress state. In contrast, the development of wrinkle-ridge rings is best explained as the result of cooling and contraction of Mercury's interior, during which a reduction in Mercury's surface area led to a compressional state of stress. The critical factor in determining where large graben form is the thickness of the youngest cooling unit, the topmost sequence of lavas that cooled coevally. A thicker cooling unit leads to a deeper initiation of normal faulting (wider graben floors). Consistent with observations, the widest graben are predicted to occur where pooled lavas were thickest, and no graben are predicted within generally thinner plains outside of major craters. Observed concentrically oriented graben can be explained by variations in the thickness of the youngest cooling unit. In contrast, none of the basin uplift mechanisms considered, including isostatic response to crater topography, inward flow of the lower crust, or exterior loading by volcanic plains, can account for concentrically oriented graben.

Citation: Freed, A. M., D. M. Blair, T. R. Watters, C. Klimczak, P. K. Byrne, S. C. Solomon, M. T. Zuber, and H. J. Melosh (2012), On the origin of graben and ridges within and near volcanically buried craters and basins in Mercury's northern plains, *J. Geophys. Res.*, 117, E00L06, doi:10.1029/2012JE004119.

1. Introduction

[2] Since insertion into orbit about Mercury in March 2011, the MErcury Surface, Space ENvironment, GEochemistry, and Ranging (MESSENGER) spacecraft has obtained high-resolution images of Mercury's surface that have revealed features in unprecedented detail, particularly at high northern latitudes. There, a continuous expanse of smooth plains covers more than 6% of Mercury's surface area (Figure 1).

High-resolution images from orbit show embayment relations, flow features, structures interpreted to be volcanic source vents, and impact crater size-frequency distributions indicating that the northern plains are volcanic in origin [Head *et al.*, 2011]. Moreover, the lack of regional variations in surface reflectance or crater size-frequency distribution supports the inference that the emplacement of the northern plains involved high effusion rates and large erupted volumes of lava [Head *et al.*, 2011]. These characteristics are analogous to those of terrestrial flood basalts produced by the extrusion of large volumes of lava over geologically short time intervals [e.g., Coffin and Eldholm, 1993; Thordarson and Self, 1998]. This interpretation is further supported by MESSENGER X-Ray Spectrometer data indicating that the composition of the northern plains matches those of low-iron basalts [Nittler *et al.*, 2011; Weider *et al.*, 2012].

[3] Among the most remarkable features of the northern plains are impact craters and basins, up to 300 km in diameter that have been completely buried by volcanic plains material and remain visible only by rings of ridges that mark their buried rims (Figure 2). That ridge rings overlie rims of craters and basins is supported by topographic profiles obtained with MESSENGER's Mercury Laser Altimeter

¹Department of Earth, Atmospheric, and Planetary Sciences, Purdue University, West Lafayette, Indiana, USA.

²Center for Earth and Planetary Studies, Smithsonian Institution, National Air and Space Museum, Washington, D. C., USA.

³Department of Terrestrial Magnetism, Carnegie Institution of Washington, Washington, D. C., USA.

⁴Lamont-Doherty Earth Observatory, Earth Institute at Columbia University, Palisades, New York, USA.

⁵Department of Earth, Atmospheric, and Planetary Sciences, Massachusetts Institute of Technology, Cambridge, Massachusetts, USA.

Corresponding author: A. M. Freed, Department of Earth, Atmospheric, and Planetary Sciences, Purdue University, West Lafayette, IN 47907, USA. (freed@purdue.edu)

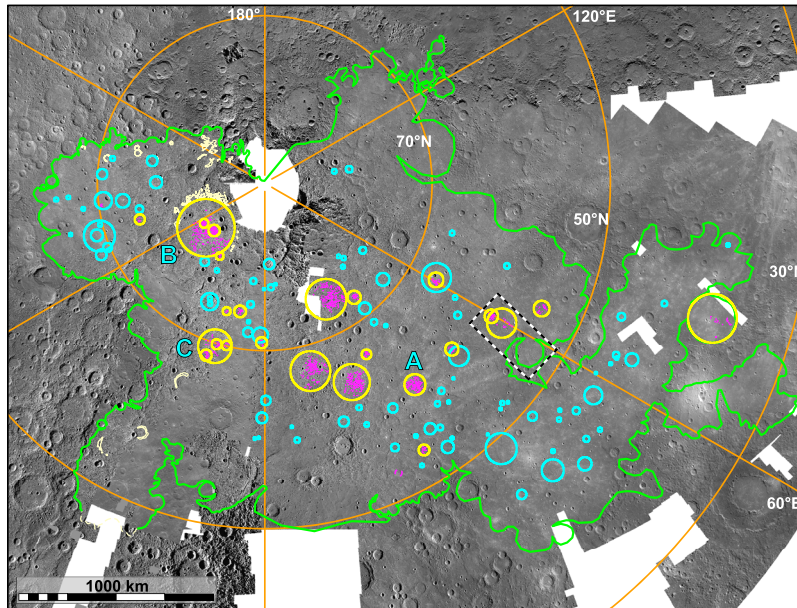


Figure 1. The volcanically emplaced northern plains of Mercury (outlined in green) as imaged by the MESSENGER Mercury Dual Imaging System (MDIS). Ghost craters and basins that host interior graben are denoted by yellow circles. Ghost craters and basins without graben are denoted by cyan circles. Graben are denoted by magenta lines. Adapted from *Head et al.* [2011] and *Watters et al.* [2012]. A, B, and C denote ghost impact features shown in more detail in Figures 2, 3, and 4, respectively. The box outlined in black/white dashed lines encloses a pair of similar-sized basins, one of which contains graben whereas the other does not.

(MLA) [Zuber *et al.*, 2012], which indicate broad topographic depressions generally concentric with the rings. These “ghost” craters and basins are distributed throughout the northern plains (Figure 1). On the basis of extensive characterization of the morphologies of impact features on Mercury [Pike, 1988; Baker *et al.*, 2011], we here use the term crater to denote an impact structure smaller than 100 km in diameter, and the term basin to denote an impact structure larger than 150 km in diameter and having at least two concentric rings, in recognition of the observation that over the intervening diameter range multiple types of crater form can be found. On the basis of their rugged morphology and high relief, the rings of ridges have been interpreted to be wrinkle ridges produced in response to horizontal compressive stresses [Watters *et al.*, 2012]. The northern plains also contain many wrinkle ridges located outside the ghost craters and basins (and a few within them); most of these ridges display no systematic orientation with respect to impact features or the plains boundary. Wrinkle ridges and other contractional landforms on Mercury have typically been attributed to the global contraction that accompanied interior cooling, to tidal despinning, or to a combination of both processes [Strom *et al.*, 1975; Solomon, 1977; Melosh and Dzurisin, 1978; Melosh and McKinnon, 1988; Watters *et al.*, 1998, 2004; Hauck *et al.*, 2004; Dombard and Hauck, 2008; Matsuyama and Nimmo, 2009].

[4] Within some of the ghost craters and basins are families of troughs interpreted to be graben produced in response to horizontal extensional stress (Figure 2) [Watters *et al.*, 2012]. No graben are seen in the northern plains outside of the ghost impact features. Inside some of the largest ghost basins are ghost craters, within which graben exhibit the

largest extensional strains [Klimczak *et al.*, 2012]. Ghost craters and basins contain graben with a variety of orientations, including circumferential at the outer margin, radial somewhat inward of the rim, and with multiple orientations and arrayed so as to form polygonal patterns closer to the crater center (Figure 3).

[5] The pattern of faulting within ghost basins and craters in Mercury’s northern plains differs markedly from that within lunar mascon mare basins. In general, mare basins display graben only on the outskirts of the basins, and the graben are often seen outboard of mare fill and outside the basin rim. Wrinkle ridges are generally found interior to the graben, though there is often an overlap in the distribution of the two feature types with radial distance from the basin center [Solomon and Head, 1980]. This faulting pattern in lunar mascon maria has been modeled as the result of volcanic loading and subsidence of the lithosphere, which induces compressional stresses (and thus wrinkle ridges) in the basin interior and extensional stresses (and thus graben) by lithospheric flexure [Melosh, 1978]. Overlap in the radial distance of wrinkle ridges and graben is inferred to be the result of a change in lithospheric thickness during an extended period of basalt emplacement and interior cooling [Solomon and Head, 1980; Freed *et al.*, 2001]. The relative locations of ridges and graben in the ghost craters and basins of Mercury’s northern plains, however, is opposite to that which would be expected from subsidence induced by volcanic loading of impact depressions. One possibility is that the graben were produced by uplift, perhaps by isostatic adjustment or lower crustal flow in response to basin topographic relief [e.g., Watters *et al.*, 2005].

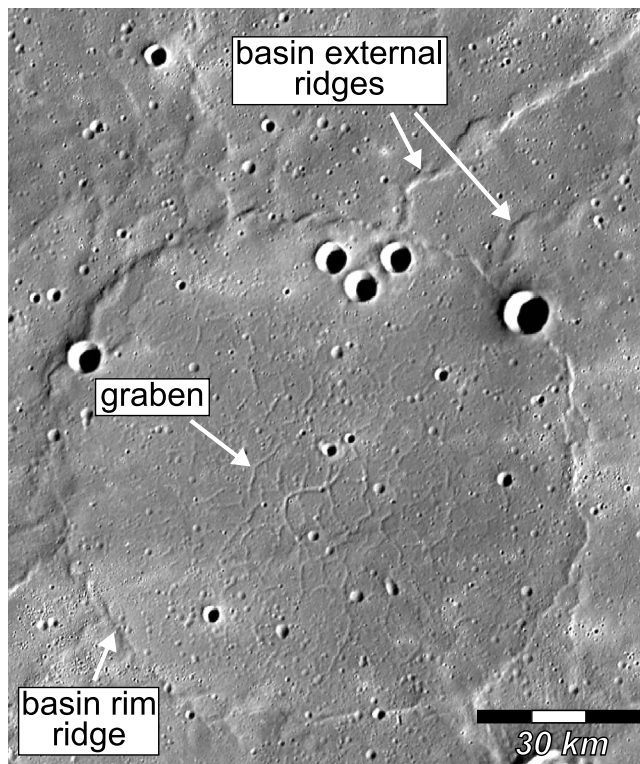


Figure 2. Image of a ghost impact crater on Mercury's northern plains (crater A in Figure 1). The rim of this volcanically buried crater is marked by a wrinkle-ridge ring ~ 100 km in diameter. Other wrinkle ridges are seen outside the crater. Within the crater are a number of troughs interpreted to be graben produced in response to horizontal extension [after *Watters et al.*, 2012].

[6] An alternative possibility is that the patterns of tectonic landforms within ghost craters and basins on Mercury are related to infilling of the impact features by flood lavas. The spectral and morphological homogeneity of the northern plains suggests that much or all of the plains unit may have been emplaced in a few very large volcanic events, in contrast to mineralogically distinct flows in lunar mare basins that indicate emplacement by multiple smaller events over an extended period of time [e.g., *Hiesinger et al.*, 2011]. High effusion rates combined with low-viscosity flows in the northern plains of Mercury may have led to greater pooling of lavas, especially within impact basins, resulting in thicker cooling units compared with those in lunar mare basins. The formation of graben within ghost basins may therefore be tied to the thermal contraction of these thicker cooling units.

[7] In this paper, we seek to test several candidate mechanisms for the formation of ridges and graben associated with ghost craters and basins in Mercury's northern plains. To this end we develop finite element models to simulate these processes in order to determine the stress state that each mechanism would likely produce. These stress states can then be compared with those implied by the observed faulting styles. Plausible scenarios must explain not only the patterns of graben that are observed, but also why graben are not observed in all buried craters and basins,

including situations where graben appear in only one of two neighboring basins of similar size (Figure 1). In addition, a successful candidate process must explain why such patterns of faulting are not observed in lunar mare basins.

2. Observational Constraints

[8] As a first step in testing formational scenarios for the patterns of faulting observed in and around ghost basins and craters in the northern volcanic plains of Mercury, we summarize the six primary observational constraints against which models should be tested.

[9] (1) *Wrinkle-ridge rings*. Most buried basins and buried craters outside of basins are marked by a wrinkle-ridge ring presumed to outline the buried rim (Figure 2). Measurements made by MESSENGER's Mercury Laser Altimeter [*Zuber et al.*, 2012] indicate that these ridges generally rise 200–400 m above the surrounding plains and 400–900 m above the center of the ghost crater or basin they encircle [*Klimczak et al.*, 2012]. The differences in elevation between the floors of the ghost craters or basins and the surrounding plains reveals that although the impact features are completely covered by volcanic deposits, some remnant of an impact depression remains.

[10] (2) *Exterior ridges*. Many ridges are observed in the smooth plains outside of the ghost craters and basins. These exterior ridges have elevations that are generally less than those of the ridge rings, although in some cases they approach the same height. The exterior ridges display a variety of orientations, but they often exhibit basin-radial orientations as they approach a ridge ring (Figure 2). Most of these exterior ridges are interpreted as wrinkle ridges [*Watters et al.*, 2012], but a few have also been interpreted as lava flow fronts [*Head et al.*, 2011].

[11] (3) *Interior ridges*. Two categories of ridges are seen within ghost basins. The first are smooth, low-lying ridges associated with the rims of buried interior craters (e.g., Figure 3). Altimeter measurements show that these ridges rise only about 50 m above the surrounding plains. The second are wrinkle ridges, interpreted as such on the basis of their rugged morphology and higher elevations. At least one of these ridges is observed to cross a wrinkle-ridge ring

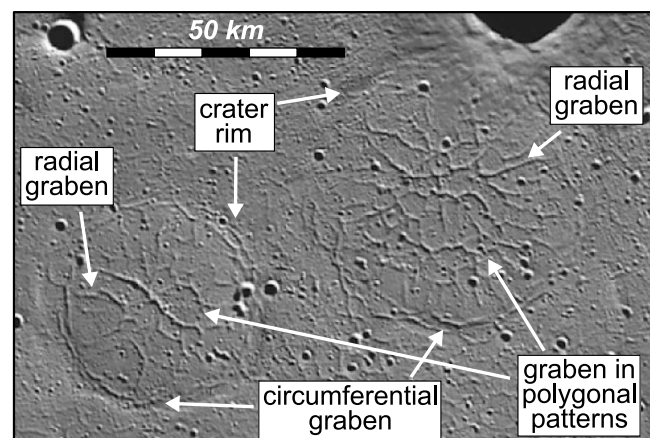


Figure 3. Two ghost craters interior to the Goethe basin (basin B in Figure 1), and associated tectonic structures. The craters have diameters of ~ 47 and 60 km.

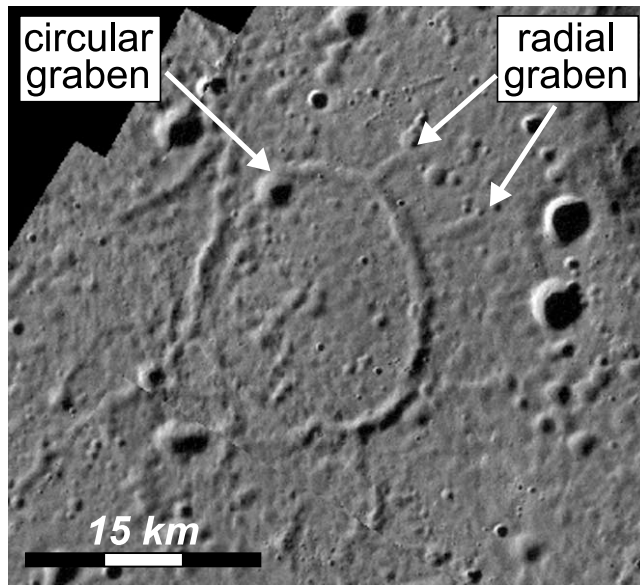


Figure 4. A graben ring interpreted as marking the buried rim of a small ghost crater, with radially oriented graben extending outward. The ghost crater lies within the 170-km-diameter basin C in Figure 1.

[Watters *et al.*, 2012], though the age relationship between these two ridges cannot be readily determined. There are only a few basin-interior wrinkle ridges, fewer per area than are observed external to the basins.

[12] (4) *Ghost-basin graben.* Graben observed within ghost basins have widths that are greatest near the basin centers and decrease with radial distance from the basin center until they are barely visible near the basin rim. No preferred graben orientations are discernible, with basin-radial and basin-circumferential graben intersecting to form polygonal patterns (Figure 2). Floor widths range from about 0.2 to 0.6 km and rim-to-rim widths range from about 0.8 to 1.2 km [Klimczak *et al.*, 2012]. This distinction is important, because according to some models [e.g., Melosh and Williams, 1989] graben floor widths are unlikely to have changed markedly with time, whereas rim-to-rim widths may have continued to grow as strain was accommodated. Thus, it is the difference between these two measurements that is indicative of total strain accommodation. Moreover, geological and numerical studies have shown that graben-bounding normal faults generally have dip angles of $\sim 60^\circ$ and meet at depth, with this depth indicative of the minimum thickness of the mechanical layer in which extensional stresses were concentrated [Melosh and Williams, 1989; Schultz *et al.*, 2007]. Although it is an oversimplification to assume that the width of the graben floor corresponds directly to the depth of the deforming mechanical layer (i.e., the youngest cooling unit), we interpret wider graben floors as indicative of a thicker cooling unit and vice versa.

[13] (5) *Ghost-crater graben.* Graben in ghost craters within ghost basins tend to have larger widths and more regions with a prevalent fault orientation than other basin graben. As with basin graben, the widest graben in ghost craters interior to ghost basins are found near the crater center, and widths diminish with distance from the center

(Figure 3). Graben floor widths near the centers of the craters are 0.6–1.0 km, whereas rim-to-rim widths are 1.4–1.8 km. Both values are larger than for other graben that lie within the ghost basins but are outside the interior ghost craters. In a manner similar to the situation in ghost basins, graben near the centers of ghost craters show no preferred orientation and instead form polygonal patterns. Outward from the center, some graben have a basin-radial orientation, but immediately inward of the rim circumferentially oriented graben are most often observed (Figure 3). Several small ghost craters (10–15 km diameter) are evident by a graben ring that appears to overlie the rim [Klimczak *et al.*, 2012]; at some graben rings are spoke-like radial graben that extend outward (Figure 4).

[14] (6) *Distribution of graben-hosting ghost craters and basins.* Most ghost craters and basins that contain graben are located near the center of the northern plains (Figure 1), and most of these are at least 100 km in diameter, though a few smaller craters outside of basins also contain graben. A notable exception is a relatively large basin located near the southern edge of the plains. Also of interest is a basin without graben located very near a basin of similar size that hosts graben (Figure 1). Such a pair of neighboring features poses another constraint on candidate processes.

3. Modeling Approach

[15] The style of faulting and the orientation of tectonic landforms with respect to the basin or crater center reveal the stress state that existed when faulting was initiated. Specifically, the relative magnitudes of the three principal stresses determine the style of faulting [Anderson, 1951]. Because volcanic units are near the surface, one of the principal stresses will invariably be oriented close to vertical, and the other two principal directions will be nearly horizontal. It is the magnitude of the vertical stress relative to the two horizontal principal stresses that determines if the faulting will be extensional (vertical stress is the most compressive) or compressional (vertical stress is the least compressive), and the relative magnitude of the two horizontal principal stresses determines the orientation of faulting (Table 1). For example, graben oriented circumferentially with respect to a basin or crater center imply a stress state given by $\sigma_r > \sigma_c > \sigma_v$, where σ_r , σ_c , and σ_v are the radial, circumferential, and vertical principal stresses, respectively, and where compressive stress is defined as negative. We assume that irregular fault orientations, such as when radially and circumferentially oriented

Table 1. Styles of Faulting Predicted From the Relative Magnitude of the Principal Stress Components With Respect to the Center of a Basin or Crater^a

Relative Magnitudes	Stress State	Predicted Style of Faulting
$\sigma_r > \sigma_c > \sigma_v$	extensional	circumferential graben
$\sigma_r \approx \sigma_c > \sigma_v$	extensional	unoriented graben
$\sigma_c > \sigma_r > \sigma_v$	extensional	radial graben
$\sigma_c > \sigma_v > \sigma_r$	shear	strike-slip faulting
$\sigma_r > \sigma_v > \sigma_c$	shear	strike-slip faulting
$\sigma_v > \sigma_c > \sigma_r$	compressional	circumferential ridges
$\sigma_v > \sigma_c \approx \sigma_r$	compressional	unoriented ridges
$\sigma_v > \sigma_r > \sigma_c$	compressional	radial ridges

^aCompressive stresses are negative; σ_r is radial stress, σ_c is circumferential stress, and σ_v is vertical stress.

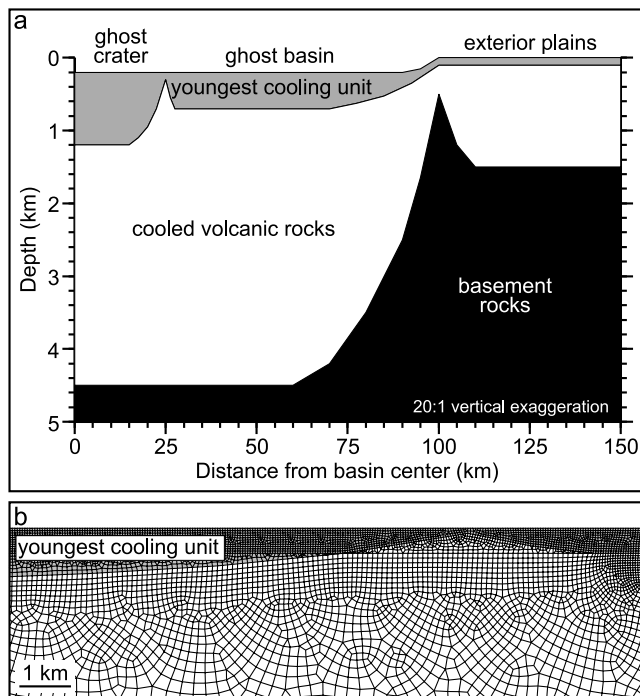


Figure 5. (a) Schematic cross section of modeled ghost basin and ghost crater adopted in this study and (b) a small portion of an axisymmetric finite element mesh showing the edge of a ghost crater (25 km radius) within a ghost basin (100 km radius).

graben intersect to delineate polygonal patterns, are representative of a stress state in which the radial and circumferential stress components are of similar magnitude.

[16] With the general stress state at the time of faulting determined from the faulting style, our analysis objective was to determine which candidate process would have led to that state of stress. This objective was accomplished by developing finite element models capable of specifying the stress state for each scenario under a given set of modeling assumptions. Models are capable of determining only that stress state that may have led to the faulting styles observed; it is beyond the scope of this analysis to simulate fault initiation or development. We used the finite element code Abaqus, which is in widespread use for mechanical and thermal engineering simulations (<http://www.simulia.com>) and has been successfully employed to simulate a variety of terrestrial tectonic processes [e.g., Freed et al., 2010] and in impact basin deformation simulations, such as a study that addressed the origin of the Pantheon Fossae system of radial graben in the Caloris basin [Freed et al., 2009].

[17] We took advantage of basin and crater axisymmetry to simplify modeling requirements. Figure 5 shows an example of a model geometry considered in our analysis and a corresponding axisymmetric finite element mesh of a crater with a radius of 25 km at the center of a basin of radius 100 km. This configuration was a matter of modeling convenience; the centers of ghost basins and any interior ghost craters generally do not coincide, but observations of faulting within ghost craters suggest that the placement of the crater within a basin is not an important consideration. Model domains and mesh resolution varied and depended on the

process being simulated. Models for which operating processes were confined to the upper crust (global contraction and thermal contraction of youngest cooling unit) extended 20 km in depth and 300 km in radius, and models that treated lithospheric flexure and viscous flow (isostatic uplift, lower crustal flow, and exterior basin loading) extended to 200 km depth and 1000 km in radius from the basin center.

[18] Axisymmetric boundary conditions were applied to the basin's central axis, and fixed (zero displacement) boundary conditions were applied to the distal side and bottom boundaries. The locations of the fixed boundary conditions were tested to ensure that they did not markedly influence calculated stress fields in the vicinity of the modeled basin. Except where specified, we adopted the nominal model parameters listed in Table 2. From measured depth-to-diameter ratios for impact craters and basins on Mercury [Barnouin et al., 2012], we adopted a depth of 3 km below the basin rim for the sub-volcanic basin-floor of a 200-km-diameter basin and a floor depth of 1 km below the crater rim for an interior 50-km-diameter crater (Figure 5). We assumed that the floor of either impact feature is flat to a radial distance of two-thirds of the radius to the rim and then shoals smoothly to the rim. This geometry enabled us to explore the influence of both flat and curved basement floor geometry on the distribution of stresses within the volcanic fill for the various scenarios modeled. Ghost craters larger than ~ 10 km in diameter were presumably formed with a central peak [Pike, 1988]. The presence of a central peak would not have affected the results of uplift models, as stresses are primarily influenced by lithospheric thickness. For cooling models, a thinner cooling unit at the very center of a ghost crater would have led to greater thermal stresses, but such a geometry would not have influenced the relative magnitude of the stress components (from which we predict faulting styles), as continuum mechanics requires that both horizontal stress components be equal at the basin center.

[19] For models that included both a lithosphere and an asthenosphere (i.e., models for uplift scenarios), the lithosphere was treated as elastic and the asthenosphere was assumed to be viscoelastic with a viscosity of 10^{20} Pa s. Results are not sensitive to the viscosity, because the calculated stress state of the volcanic fill was taken after a steady

Table 2. Model Parameters Adopted for This Analysis

Symbol	Description	Value	Units
ρ_f	Density of volcanic fill	3200	kg m ⁻³
ρ_c	Density of crust	3200	kg m ⁻³
ρ_m	Density of mantle	3400	kg m ⁻³
E	Young's modulus	10^{11}	Pa
	(in all regions unless specified in the text)		
ν	Poisson's ratio	0.25	
η_{lc}	Viscosity of lower crust	10^{20}	Pa s
η_a	Viscosity of asthenosphere	10^{20}	Pa s
g	Gravitational acceleration	3.7	m s ⁻²
T_s	Surface temperature	0	°C
ΔT	Background thermal gradient	10	°C km ⁻¹
T_b	Elastic blocking temperature of fill	900	°C
κ_f	Thermal conductivity of fill	1.5	W m ⁻¹ K ⁻¹
κ_b	Thermal conductivity of basement	0.5–1.5	W m ⁻¹ K ⁻¹
α_f	Volumetric coefficient of thermal expansion	3×10^{-5}	°C ⁻¹

state condition had been achieved (i.e., after the asthenosphere had completely relaxed). We adopted a crustal density of 3200 kg/m^3 , on the basis of an inferred mafic composition indicated by X-ray spectrometry [Nittler *et al.*, 2011], and a mantle density of 3400 kg/m^3 . The density of the volcanic plains material was assumed to equal the crustal density on the basis of similarities in color and implied similarities in composition to older crustal units [Denevi *et al.*, 2009]. For models with a lithosphere thinner than the crust, the crust below the base of the lithosphere was taken to be viscoelastic with the same viscosity as the asthenosphere.

[20] Models that treated local cooling included conductive cooling of an initially hot layer of fill overlying cool older flows. These calculations required an assumed background thermal structure. However, surface temperatures on Mercury have substantial latitudinal and longitudinal variations [Vasavada *et al.*, 1999]. On the basis of the diurnal average surface temperature at the equator and the expected variation with latitude [Vasavada *et al.*, 1999], we adopted a surface temperature of 0°C as representative of the northern plains. We assumed a thermal gradient with depth of 10°C/km [Watters *et al.*, 2002; Hauck *et al.*, 2004; Zuber *et al.*, 2010]. Cooling was assumed to be from an initial temperature of 900°C , an estimate of the elastic blocking temperature at which thermal stresses can begin to accumulate [e.g., Hirth, 2002]. It is the net temperature drop—the difference between the modeled initial and background temperatures—that determines the magnitude of thermal contraction. Though there is considerable uncertainty in these temperatures and the resulting absolute stress levels, the uncertainty does not extend to the relative magnitudes of the thermal stress components from which predicted faulting styles are determined. The relative magnitudes of the thermal stress components are influenced primarily by the shape of the cooling unit.

4. Testing of Candidate Processes

4.1. Uplift During Isostatic Response

[21] If ghost basin topographic relief were initially undercompensated, then the crust beneath the basin would have risen until the mass deficit was balanced by flexural stresses in the lithosphere (Figure 6a). This uplift would have led to horizontal extensional stresses within the basin, potentially accounting for the formation of graben. We have modeled isostatic uplift for an uncompensated basin (flat initial topography along the crust–mantle boundary), with a lithospheric thickness that is treated as a variable within the range 25 to 100 km. At the surface, the centers of volcanically filled ghost basins on Mercury lie $\sim 0.5 \text{ km}$ below the surrounding plains [Klimczak *et al.*, 2012]. Under the application of gravity, isostatic body forces drive the basin upwards until basin topography is balanced between isostatic forces and lithospheric stresses. The distribution of lithospheric (flexural) stresses is controlled by the thickness of the elastic lithosphere.

[22] The calculated stress components from within the fill of a 200-km-diameter ghost basin as a result of isostatic uplift with a lithospheric thickness of 25 km are shown in Figure 7. Uplift of the basin places it in a state of horizontal extension, and the similar magnitudes of the radial and circumferential stress components near the basin center are consistent with an observed lack of preferential orientation of graben (e.g., bounding polygonally shaped blocks) near

the basin center. However, the isostatic uplift model cannot explain why graben are generally found to have greater widths in ghost craters within basins, and it cannot account for the generation of circumferentially oriented graben. Away from the crater center, calculations show that the circumferential stress becomes more extensional than the radial stress component (Figure 7), which would lead to radially oriented graben. Such orientations are consistent with those observed for graben in the outer regions of some ghost craters (e.g., Figure 3). However, the isostatic uplift model predicts that radial graben should also have formed well beyond the rims of these ghost craters, where they are not observed.

[23] An additional issue with isostatic uplift as a mechanism for graben formation is that to generate substantial stresses this process would have to have been incomplete at the time of emplacement of the volcanic plains. This timing implies that all of the ghost basins with graben must have formed at about the same time and shortly before northern plains volcanism, a coincidence of low probability. Moreover, impact basins on the Moon tend to be isostatically overcompensated [Neumann *et al.*, 1996; Namiki *et al.*, 2009] rather than undercompensated, making this mechanism unlikely if basins on Mercury formed in a similar manner.

4.2. Uplift During Lower Crustal Inflow

[24] A consequence of isostatic support of basin topography due to an uplifted crust–mantle boundary is that the overburden pressure within the crust outside the basin is greater than that beneath the basin for depths shallower than the depth of compensation. This pressure difference can drive inward flow of the lower crust toward the basin center, causing uplift of the basin and a relaxation of basin topography (Figure 6b) [e.g., Zhong, 1997; Watters *et al.*, 2005]. If extensional stresses associated with uplift are sufficient to induce normal faulting, this mechanism could potentially account for the origin of graben in ghost basins. Moreover, if flexural subsidence outward of the uplifted region coincides with the location of the basin rim, this process could potentially be responsible for the formation of wrinkle ridges along the basin rim.

[25] Lower crustal flow models were run in the same fashion as for the isostatic models, with body forces arising from gravity acting on density contrasts serving to drive the deformation. We assumed a crustal thickness of 100 km outside the basin and a variety of depths (15–70 km) to the brittle–ductile transition within the crust. Though this adopted crustal thickness is likely larger than appropriate for Mercury [Smith *et al.*, 2012], such an assumption maximizes the potential influence of lower crustal flow on basin uplift. The viscosity of the lower crust was assumed to be 10^{20} Pa s , though as with the asthenosphere in isostatic models, this value does not influence calculated steady state stresses. We utilized an abrupt brittle–ductile transition as a matter of modeling convenience—any steady state stress results within the volcanic fill from a depth-dependent or even a stress-dependent viscosity structure can be matched by adjusting the depth of a single abrupt transition. If the mantle were modeled with a viscosity lower than that for the lower crust, then about half of the lower crustal flow field would turn downward beneath the basin to accommodate flowing mantle, rather than working to uplift the basin. To maximize the

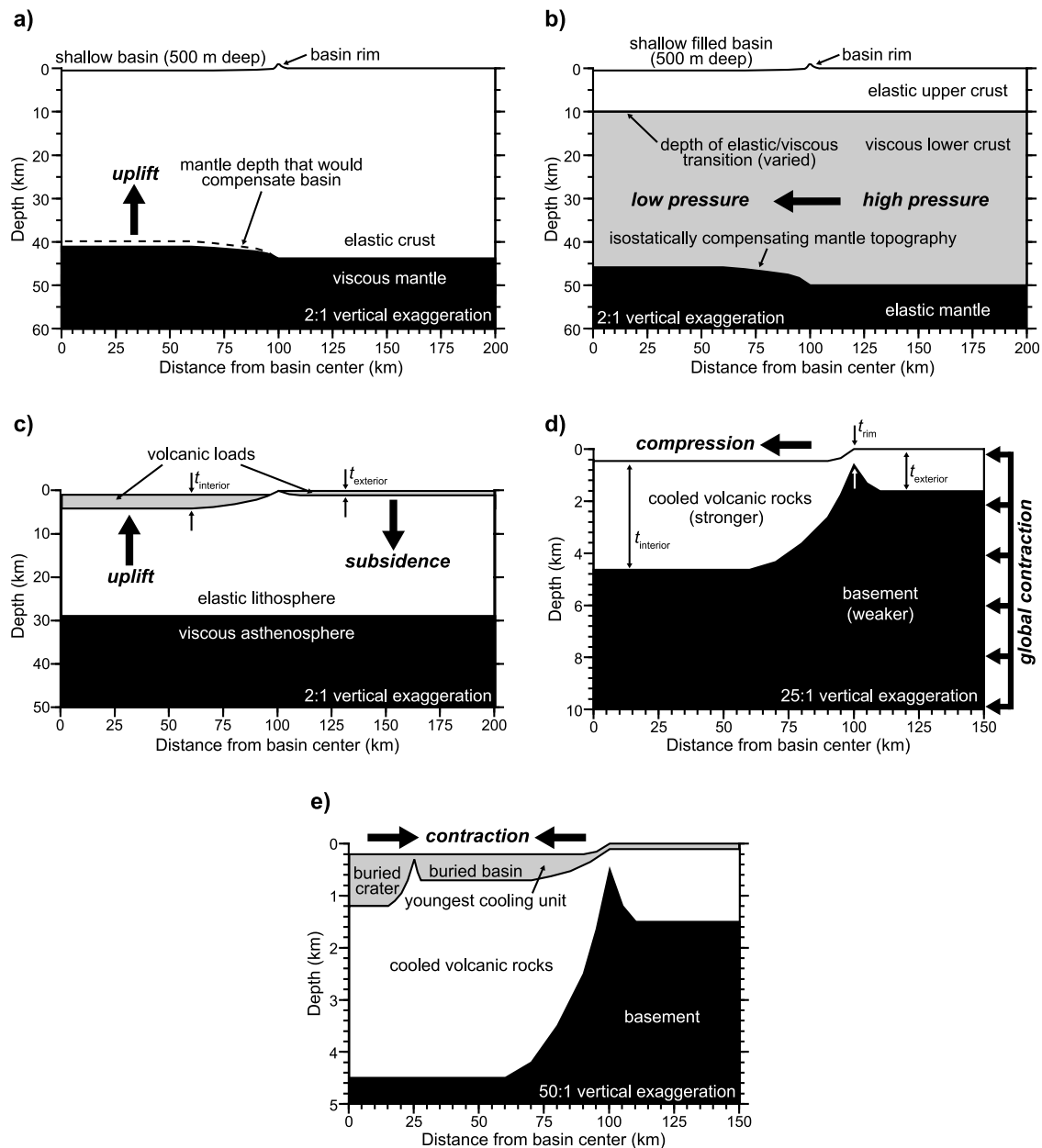


Figure 6. Schematic illustrations of candidate mechanisms for graben formation on the floors of ghost basins and craters: (a) uplift due to an isostatic undercompensation of the impact structure following excavation, (b) uplift in response to inward flow of the lower crust, (c) uplift in response to exterior volcanic loading, (d) compression due to global contraction, and (e) cooling and contraction of the youngest cooling unit. All illustrations show an axisymmetric basin with the axis of symmetry at the left edge. In all models, the cumulative thickness of volcanic material within the basin ($t_{interior}$) is substantially greater than that exterior to the basin ($t_{exterior}$), and the thickness over the buried basin rim (t_{rim}) is less than either inward or outward of the rim.

potential influence of lower crustal flow, we modeled the mantle as elastic in these models.

[26] Calculated stress components produced by uplift in response to lower crustal flow for a model with a thin (15 km) elastic lithosphere are shown in Figure 8. The resulting stress state is similar to that for an isostatic uplift model with a similarly thin lithosphere. Graben are predicted to form more readily in basin centers, where they should have no preferred orientation. As with the uplift models, this

model cannot explain either the distribution of graben widths in ghost craters or the formation of circumferentially oriented graben. This model also cannot be used to account for the generation of ridges at basin rims, as thrust faulting is not predicted to occur until well outside the basin and is not focused at the basin rims. Although a particular choice of model parameters may yield a set that leads to compression at a radial distance coincident with a given rim radius, one

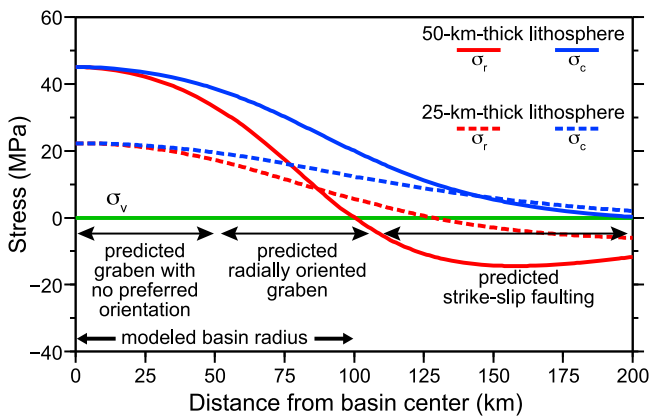


Figure 7. Calculated stress components near the top of basin fill for an isostatic uplift model and lithospheric thicknesses of 25 and 50 km. Predicted styles of faulting derived from the relative magnitude of the stresses (Table 1) are noted.

set of parameters will be inadequate to explain ridge formation over a wide range of basin rim diameters.

[27] Especially problematic for a lower crustal flow scenario is the fact that a very shallow brittle–ductile transition (~ 15 km or less) is required to achieve a stress state in which differential stresses are at least at the level of tens of MPa. For example, a model with a brittle–ductile transition at 40 km depth leads to differential stresses of only 6 MPa near the basin center. A 15-km-deep brittle–ductile transition would be difficult to explain in terms of likely thermal gradients [e.g., *Hauck et al.*, 2004], and the probable lack of crustal water, which serves as a rheological weakening agent on Earth. For an average surface temperature in the northern plains of 0°C and a $10^\circ\text{C}/\text{km}$ thermal gradient, the temperature at 15 km depth in the northern plains is probably only $\sim 150^\circ\text{C}$, too low for crustal rocks (particularly mafic rocks) to flow viscously even under hydrous conditions [e.g., *Hirth*, 2002]. Although there is considerable variability and uncertainty in thermal structure (as discussed above), temperatures would have to be many hundreds of degrees warmer in order for viscoelastic flow to occur at such shallow depths.

[28] As with the isostatic uplift scenario, the lower crustal flow scenario requires that the volcanic plains were emplaced shortly after crater excavation, implying that the graben-hosting ghost craters and basins are all of similar age. Moreover, the amplitude and wavelength of flexural stresses associated with lower crustal flow are dependent on the assumed depth of the brittle–ductile transition within the crust. For their lower crustal flow model for the 1500-km-diameter Caloris basin, *Watters et al.* [2005] assumed that this depth was ~ 50 km on the basis of temperature-dependent rheological arguments. For the smaller basins and craters in the northern plains, a much shallower brittle–ductile transition (leading to a shorter flexural wavelength) would be required to explain why graben are observed only inside the basins, rather than outside as well, and to account for the formation of wrinkle ridges along the basin rim. The flexural wavelength would also have to vary so as to scale with the diameter of each impact feature, an improbable situation.

4.3. Uplift From Exterior Volcanic Loading

[29] The emplacement of extensive volcanic plains exterior to the Caloris basin has been proposed as a mechanism for the formation of graben in the interior plains of that basin [*Melosh and McKinnon*, 1988; *Kennedy et al.*, 2008; *Freed et al.*, 2009]. In this scenario, subsidence in response to these exterior lithospheric loads causes flexural uplift of the basin, placing the basin interior in a state of extension (Figure 6c). If applied to ghost basins, such a scenario would require that the flexural forces that drive the basin interior upwards in response to external loading must have exceeded the downward forces imparted by basin infill. This could be the case if the exterior plains are sufficiently thick or if a late stage of basin-exterior volcanism occurred after completion of subsidence from earlier flows that filled the basin interior. However, whereas the plains exterior to the Caloris basin are inferred to be somewhat younger than the interior plains [*Fassett et al.*, 2009], a similar relative timing does not appear to apply to the buried basins in the northern plains. Nonetheless, we include here a model for the style of faulting that external volcanic loading would impart to ghost basins.

[30] Exterior volcanic loading models utilize the isostatically compensated geometry of the lower crustal flow model, but with a 500-m-thick volcanic unit added just outside the basin rim to represent a possible final episode of volcanism. A different assumption for thickness of this exterior flow would influence the magnitude of the resulting stresses but not the relative magnitudes of the stress components, which are influenced primarily by the assumed lithospheric thickness, treated as a variable.

[31] Calculated stress components produced by uplift in response to exterior loading for a lithospheric thickness of 50 km are shown in Figure 9. Graben without a preferred orientation are predicted to form near the basin center, and radially oriented graben are predicted away from the basin center, as was found for the other modeled uplift scenarios. In a like manner, exterior basin loading is not capable of accounting for circumferentially oriented graben or the distribution of graben throughout the interiors of ghost craters and basins. In addition, high differential stresses beyond the 200-km-diameter basin rim would suggest that graben should

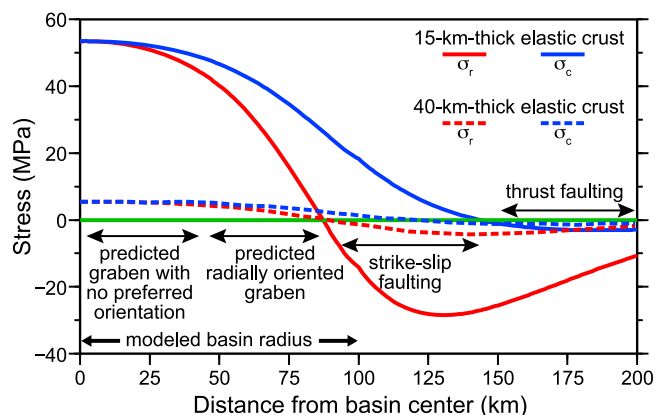


Figure 8. Calculated stress components near the top of basin fill for inward flow of the crust at depths greater than 15 and 40 km and associated basin uplift following basin formation.

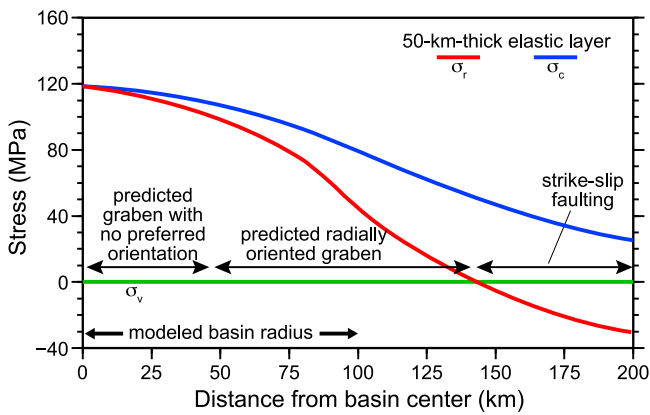


Figure 9. Calculated stress components near the top of basin fill as a result of volcanic loading by exterior plains. Subsidence of exterior plains is accompanied by uplift of the basin interior.

have formed exterior to most ghost basins, though none is observed.

4.4. Global Contraction

[32] Global contraction results from the secular cooling of a planet's interior. From early estimates of the cumulative shortening accommodated by lobate scarps on Mercury, reduction of the planetary radius of 1–2 km since the end of late heavy bombardment has been estimated [Strom *et al.*, 1975; Watters *et al.*, 1998, 2009], although most thermal history models have indicated greater contraction over this time interval [e.g., Solomon, 1977, 1978; Hauck *et al.*, 2004]. The processes of interior cooling and contraction likely were active through a large fraction of Mercury's history and would have placed the entire lithosphere into horizontal compression (Figure 6d), providing an efficient mechanism for the formation and development of wrinkle ridges and lobate scarps across Mercury's surface. Where the lithosphere was thinnest, compressional stresses would have been greatest, because contraction would have been accommodated over a smaller cross-sectional area. If the volcanic northern plains were substantially stronger than the basement rocks they overlie, then contractional stresses would have concentrated within these volcanic units, making these relatively thin plains particularly susceptible to the formation of wrinkle ridges. A strength contrast between the volcanic unit and the underlying basement rocks is likely, as the latter were fractured and gardenized by impacts prior to plains emplacement [e.g., Ahrens *et al.*, 2001].

[33] In models of global contraction, the entire volcanic unit and underlying crust were assumed to be compressed by a horizontal strain associated with 1 km of global radial contraction. This contraction corresponds to a strain of 4×10^{-4} , which is applied as a lateral displacement to the far-field horizontal boundary of the model. The key parameters in this calculation are the shape of the volcanic unit and the relative elastic strengths of the volcanic unit and the surrounding crust. We assumed that the elastic strength of the volcanic unit is greater than that of the underlying crust by a factor of 10. Different assumptions regarding this ratio influence the absolute magnitude of stresses in the crust but

not the relative magnitude of the stress components (except in the case of a ratio of 1, in which case there would be no localization of stress by basin topography). With a strength contrast between the volcanic and underlying units, lateral compressive stresses are of greatest magnitude where the volcanic unit is thinnest, above the rims of the ghost craters and basins (Figure 10a). In addition, the bending stresses associated with asymmetry of the thickness of volcanic material above the rims causes the basin-radial stress component to be notably more compressive than the basin-circumferential component. This difference favors circumferentially oriented wrinkle ridges around the edge of the basin, just above the rim, in general agreement with observations.

[34] As compressive stresses are also substantial (>50 MPa) outside of ghost craters and basins, one would also expect wrinkle ridges to form within these exterior volcanic plains. However, with minimal difference between the magnitudes of the radial and circumferential components, there would be no preferred orientation for such ridges. This prediction is consistent with observations, with the exception that basin-exterior wrinkle ridges are often observed to rotate toward a basin-radial orientation as they approach ghost basins. This pattern can be explained by stress relief at the basin rims. The wrinkle-ridge rings overlying buried rims will tend to relieve the basin-radial stresses component, leaving the basin-circumferential stress component as the most compressive stress component just outside the rim. Thus, wrinkle ridges that form farther outboard of the ghost basins but propagate into the vicinity of the basins will likely rotate toward a basin-radial orientation as the basin is approached, as appears to have been the case for the wrinkle ridge in the top right corner of Figure 2. Compressive stresses within ghost craters and basins are calculated to be somewhat lower than in exterior regions, and stress relief associated with the wrinkle-ridge ring at basin and crater rims would have further lowered interior compressive stresses, perhaps accounting for

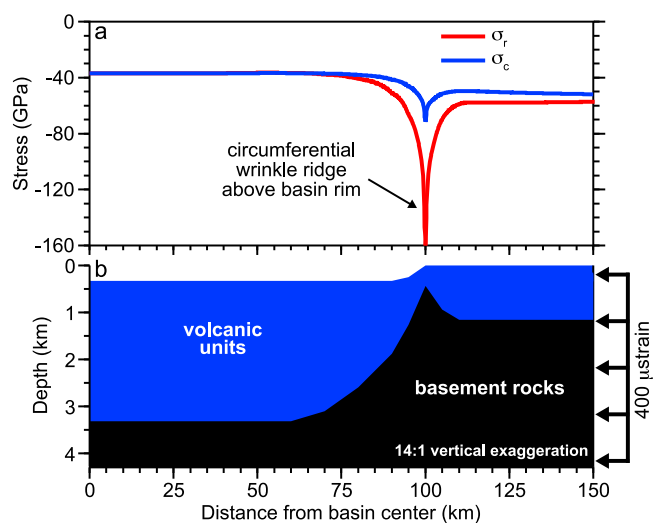


Figure 10. (a) Calculated near-surface compressional stress components resulting from global contraction. Vertical stresses near the surface are negligible. (b) Geometry of basin components and far-field boundary condition used to simulate global contraction.

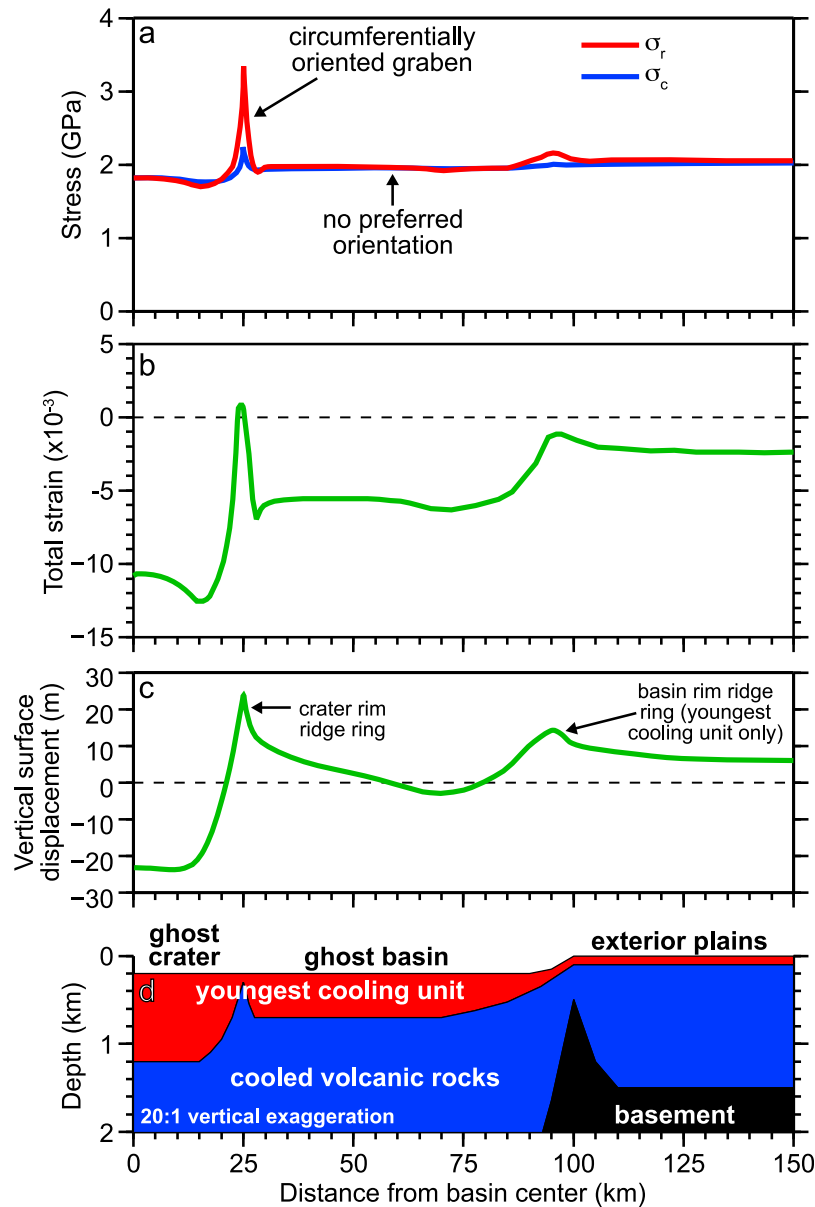


Figure 11. Calculated (a) thermal stress components and (b) total strain at median depth in the youngest cooling unit as a result of contraction from flood lava cooling. (c) Calculated vertical displacements at the surface. (d) Adopted cross section of basin and interior crater. Vertical stresses in the youngest cooling unit are negligible compared with the lateral stress components. Results shown here are for a model in which the youngest cooling unit has an elastic strength that is a factor of 10 greater than that of the underlying cooled volcanic units.

the fewer wrinkle ridges per unit area observed within ghost impact features than in plains outside of such features.

4.5. Thermal Contraction of Cooling Lavas

[35] Because younger lava flows would tend to bury faults formed on older volcanic units, calculations of thermal contraction consider only the youngest cooling unit (Figure 6e). Under the assumption that observed widths of graben floors reflect the approximate depth of this mechanically distinct layer, we modeled a youngest cooling unit of 0.5 km thickness within the modeled basin and 1 km thickness within an interior crater (Figure 5). In this scenario, a crater has formed

within a basin that has already been partially filled by lavas, and a younger layer of volcanic fill is then emplaced within the basin. This sequence results in a thicker cooling unit within the crater than the rest of the basin. Outside of the basin we assumed that the thickness of the youngest cooling unit is 0.1 km, an estimate of the maximum thickness of a cooling unit that would lead to fractures too narrow to be observable at the current resolution of global images (~ 250 m per pixel). Thermal stresses were calculated at the time at which the youngest cooling unit reached background temperatures, several tens of thousands of Earth years for a cooling unit up to 1 km thick.

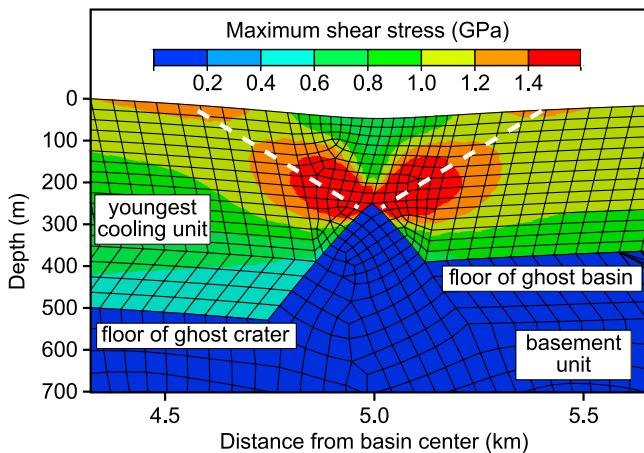


Figure 12. Finite element mesh in the vicinity of the rim of a ghost crater interior to a ghost basin showing the calculated maximum shear stresses resulting from thermal contraction of the youngest cooling unit. Exaggerated deformation of elements shows bending associated with cooling. Dashed white lines show where antithetic normal faults would develop to form a basin-circumferential graben in the volcanic unit above the rim.

[36] Thermal contraction induces a state of horizontal extension in the youngest cooling unit. Unlike global contraction, during which surface area is reduced and a compressive stress state develops, contraction of cooling lavas preserves surface area, which leads to a state of horizontal extensional stress at the surface. Generating graben from such stresses is analogous to the formation of mud cracks in drying sediments or columnar jointing in expanses of lava that cool uniformly. The magnitude of cooling stresses depends on four primary factors: the temperature drop, the coefficient of thermal contraction, the geometry of the cooling volume, and the degree to which underlying rocks provide resistance to contraction. If resistance to contraction is minimal, compressional stresses will be small, but contractional strains will be large, and vice versa. This underlying resistance, which could come from the strength of the underlying rocks or be controlled by a detachment fault, is not known. We use the ratio of the elastic strength (Young's modulus) of the youngest cooling unit to that of the underlying rocks as a proxy for whatever mechanism controlled the degree of resistance to contraction. For an elastic strength ratio of 10:1 between the cooling unit and underlying units, thermal contraction of the youngest cooling unit induces extensional stresses that can exceed 1 GPa (Figure 11a). Although fracturing and faulting would occur and relieve stress long before such stress levels could be achieved, this result underscores the ability of thermal cooling stresses to generate widespread faulting.

[37] Although the resistance to contraction by underlying units controls the magnitude of the resulting thermal stresses, the style of faulting is controlled primarily by the geometry of the youngest cooling unit. Different geometries can produce any combination of radial, circumferential, and mixed-orientation faulting (D. M. Blair et al., The origin of graben and ridges in Rachmaninoff, Raditladi, and Mozart basins, Mercury, submitted to *Journal of Geophysical Research*,

2012). For the geometry of a ghost basin and interior ghost crater shown in Figure 11d, the radial and circumferential thermal stress components are of similar magnitude in regions where the unit thickness is uniform (and would give rise to graben that lack a preferred orientation), whereas the radial stress becomes more extensional than the circumferential stress (leading to circumferential graben) in regions where the youngest cooling unit becomes thinner with increasing radial distance from the center, particularly immediately inward of the rim of a buried crater or basin (Figure 11a).

[38] The calculated stress state from thermal contraction (Figure 11a) does not explain why graben are observed within ghost basins but not within the exterior plains, as stress levels are comparable in both regions. However, a calculation of total strain (radial plus circumferential strain components) reveals that the thickness of the youngest cooling unit has a major influence on thermal strain (Figure 11b). Thicker fill leads to more than a factor of 5 greater strain in ghost craters or basins than in exterior plains. There are thus two factors that lead to larger graben in thick cooling units than the thin: deeper initiation of normal faults leads to wider graben floors, and thicker cooling units lead to higher contractional strains, which induce further growth of these initially wide graben.

[39] The initiation of circumferential graben at the edge of a ghost crater is due to two factors. One is bending of the youngest cooling unit due to its non-uniform thickness. The other is contraction of thicker cooling units on both sides of the rim that pulls the thin cooling unit over the rim into extension. Both of these effects cause the radial stress component to become more extensional than the circumferential stress component at the rim (Figure 11a). This latter effect is largest at the rims of ghost craters, because cooling units on both sides are especially thick. These extensional forces are sufficiently large to generate extensional (positive) strains at ghost crater rims (Figure 11b) despite the region generally being in a state of thermal contraction (negative strain). This effect could explain why wide circumferential graben are observed near the rims of a number of ghost craters despite the fact that the thinness of the overlying cooling unit would otherwise favor a narrow graben.

[40] The influence of a thin cooling unit being stretched by the contraction of neighboring regions with thicker fill may be most clearly evident in the wide circular graben that are observed above what are presumably the rims of small (10–20 km diameter) ghost craters (Figure 4). Contraction associated with the youngest cooling unit surrounding a ghost crater rim leads to high shear stresses along two antithetic planes and the formation of a graben (Figure 12). This circumferentially oriented graben relieves primarily radial stresses. This relief then leaves circumferential stresses the most extensional stress component in the regions surrounding the rim, leading to the formation of radially oriented graben in this region under with further contraction. Thus, thermal contraction should lead to a circular graben surrounded by radial graben, as observed at several locations in the northern plains (Figure 4). Such stress relief could also account for the presence of radially oriented graben immediately inward of circumferential graben near the rims of many ghost craters (Figure 3), as well as the formation of graben having multiple orientations in stress regimes characterized by quasi-isotropic horizontal stresses, such as near the centers of ghost craters and basins.

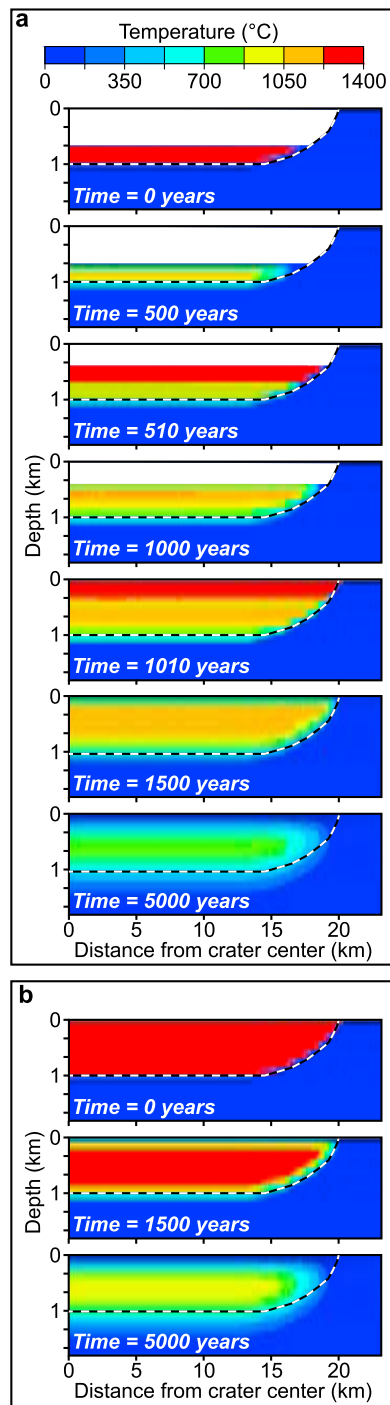


Figure 13. (a) Calculated temperatures associated with the emplacement and conductive cooling of three successive lava flows separated in time by 500 years within a 1-km-deep, 40-km-diameter impact crater. (b) Temperatures associated with conductive cooling of a single volcanic unit of the same total volume. These figures have a vertical exaggeration of 4:1.

[41] Contraction of cooling lavas also induces subsidence of the surface of the cooling unit. The magnitude of this subsidence is directly proportional to the unit thickness. Given the adopted model parameters (Table 2), calculations

indicate that for every 1 km of volcanic cover, the surface should subside by ~ 50 m. We can use this relationship to address the potential influence of thermal subsidence on the origin of ghost basin and ghost crater rims. Figure 11c shows that vertical contraction associated with cooling of the youngest cooling unit will lead to ~ 50 m of relief of a ghost crater rim above the crater floor, which compares well with MESSENGER altimeter data [Zuber *et al.*, 2012]. This agreement suggests that ghost crater rims are likely to be dominantly the result of local thermal contraction, rather than global contraction. For ghost basins, however, regional cooling cannot account for the observed relief. Models suggest that only ~ 15 m of topographic relief will be generated over the buried rim of the host basin in Figure 11d from cooling of the youngest cooling unit. Even if one considers contraction of the entire modeled 3-km-thick volcanic unit in the ghost basin, thermal subsidence will produce only ~ 150 m of rim topography, far less than the 600–900 m of relief observed at ghost basin rims. This comparison indicates that global contraction likely was the primary mechanism responsible for wrinkle-ridge topography at buried basin rims.

5. Discussion

5.1. Evolution of a Youngest Cooling Unit

[42] Results from finite element models suggest that thermal contraction of the youngest cooling unit provides the most straightforward explanation for the origin of graben within ghost craters and basins buried by Mercury's northern plains. By this mechanism, the distribution of graben within ghost craters, and their large floor widths, is predicated on the youngest cooling unit being thickest (~ 1 km) in these regions as a result of pooling of lavas. Although it may have been possible that high-volume, low-viscosity flows on the northern plains could have generated a 1-km-deep pool of lava in these craters in a single continuous eruption, this magnitude of burial would appear to outpace most single-flow events within Earth's analogous flood basalts [Thordarson and Self, 1998]. This comparison raises the question as to whether a series of individual flows separated by periods of volcanic quiescence could result in the collective flows acting as a cooling unit that contracts in a fashion similar to that of a single flow of equal thickness.

[43] In order to understand the potential for a succession of volcanic flows to cool as a single event, we modeled the filling of a 1-km-deep crater with three successive 330-m-thick flows to determine how much time could pass between flows before they are unlikely to cool as a single unit. Recall our definition of a single cooling unit is one for which the entire package of flows cools below the estimated 900°C elastic blocking temperature at more or less the same time. Each layer is initially emplaced with a temperature of 1400°C, an estimated extrusion temperature for low-iron basalt [Arndt, 2008]. The assumption of little heat loss during emplacement is consistent with the low values of inferred heat loss ($<0.1^\circ\text{C}/\text{km}$) during flow of the Columbia River flood basalts, for which an insulating crust enabled some of these flows to extend more than 300 km from their source [Thordarson and Self, 1998].

[44] Calculated temperatures following emplacement and cooling of three successive flows separated in time by

500 years are shown in Figure 13a. Despite cooling at the top and bottom boundaries of each flow, core temperatures remain above 900°C at the time of the next flow. Each successive flow then warms the top of the next older layer, serving to homogenize the thermal structure. After 500 years following the third flow (1500 years of total model time), the three-flow structure has the appearance of a single cooling unit. For comparison, Figure 13b shows calculated temperatures associated with a single volcanic flow of the same total volume. The main difference between these two calculations is that the three-flow thermal structure has cooled more in the same time period owing to surface cooling of each of the lower layers before the emplacement of younger flows. This development of a single cooling unit from successive flows begins to break down when the time period between flows becomes greater than ~1000 years, though there are trade-offs between the thickness of the individual flows and the time between flows.

[45] This result can account for the absence of graben produced by contraction of cooling lavas on the Moon; lower effusion rates, longer times between flows, and higher lava viscosities on the Moon led to the emplacement and cooling of comparatively thin individual flows rather than pooling of thick lava cooling units within impact basins. This conclusion is supported by observations of the lunar Schrödinger basin, which contains interior volcanic plains that appear to have cooled at different times, on the basis of variations in both texture and albedo [Mest, 2011]. The graben that are seen in Schrödinger also cut across the peak ring and are much longer than the graben discussed here, sometimes exceeding 100 km in length [e.g., Shoemaker *et al.*, 1994]. These observations suggest that graben within the Schrödinger basin formed in response to a regional-scale process such as uplift [Shoemaker *et al.*, 1994] and not as the result of local thermal contraction.

5.2. Distribution of Graben on the Northern Plains

[46] Model results suggest that the thickness of the youngest cooling unit is the primary factor determining locations where graben should be most prominent. This finding is consistent with the general observation that graben are found in the central region of the northern plains, as flow volumes are likely to be thickest in these regions. This relation between fill thickness and graben development could also account for why only one of two ghost basins of similar size (~150 km in diameter) and with centers only ~200 km apart has interior graben (Figure 1). The basin without graben lies on the very edge of the northern plains, and it may be inferred that the youngest cooling unit to flood this basin was not particularly thick. An outlier to these observations is a 300-km-diameter basin located near the southernmost extent of the plains (right-hand side of Figure 1), where several groupings of interior graben are observed. One can surmise that these groupings lie within interior ghost craters that are difficult to discern because relief of any topographic expression of buried rims is too small to be resolved.

[47] Most graben are located within ghost basins rather than smaller ghost craters (aside from ghost craters inside ghost basins). This result would follow if impact basins were of sufficient size to capture and pool lavas, whereas most smaller craters outside of these basins, even if they captured and pooled early lavas, were then covered fully by later lava

flows. At least some of the few small ghost craters outside of basins that contain graben may have formed shortly before cessation of northern plains volcanism and were buried only by flows of sufficient thickness to barely cover their relief.

5.3. Relative Timing of Wrinkle Ridges and Graben

[48] The relative timing of wrinkle ridge and graben formation in the northern plains is difficult to constrain, as there are few locations where the two types of landforms are observed to intersect each other with clear indications of offset. The homogeneity of the northern plains combined with inferred high effusion rates suggest that the plains were laid down over a geologically short time period. In contrast, global contraction was a slow process that spanned several billion years. Many ridges could have predated and been buried by the northern plains flows yet have later been reactivated by global contraction. Such features would predate the graben, but their surficial expression of youngest deformation may postdate the graben [Watters *et al.*, 2012]. This distinction underscores the important difference between time of formation and age of most recent activity. Model results suggest that wrinkle ridges at ghost basin rims should tend to predate other wrinkle ridges on the northern plains. This prediction follows from the higher stress levels associated with global contraction within the thin volcanic units that overlie the relic basin rim and the presumption that higher stress levels led to earlier initiation of faulting.

6. Conclusions

[49] High-resolution images of Mercury's surface by the MESSENGER spacecraft have revealed a number of tectonic landforms within the volcanic northern plains. These features include ghost craters and basins that have been completely covered by volcanic flows but are discernible because of a ring of wrinkle ridges (contractional landforms) above their buried rims. Graben (extensional landforms) are observed within many of these ghost craters and basins and accommodate the greatest strains within smaller ghost craters interior to ghost basins. Graben are observed to lack a preferred orientation near basin and crater centers but display circumferential orientations near ghost crater and basin rims. Graben rings are seen at what are presumably the buried rims of smaller craters, sometimes with radial graben extending outward from the ring.

[50] Finite element models have been developed for candidate mechanisms for the formation of wrinkle ridges and graben near and within ghost craters and basins. We tested each candidate mechanism against the stress state required to induce the observed styles and orientations of faulting. We explored a number of scenarios for uplift of ghost crater and basin interiors, including isostatic undercompensation of the impact depression, the inward flow of a viscous lower crust, and volcanic loading exterior to the crater or basin. Though these models could account for the polygonal patterns of graben seen near basin and crater centers, none predicts the formation of circumferential graben or accounts for why no graben are seen outside of ghost craters or basins.

[51] All of the principal observed characteristics of wrinkle ridges and graben in ghost craters and basins are well matched by a model of the contraction of cooling flood lavas, augmented for some wrinkle ridges by the long-term cooling

and contraction of Mercury's interior. Cooling of the interior led to a compressional stress state because of a reduction in surface area, whereas the cooling of flood lavas led to an extensional stress state because surface area was maintained. The critical factors in determining the manner by which graben formed were the thickness and shape of the youngest cooling unit, the topmost sequence of lavas that cooled below the elastic blocking temperature (the temperature at which thermal stresses can accumulate) as a single unit. A thicker youngest cooling unit leads to a deeper initiation of normal faulting (wider graben floors) as well as higher strains (larger rim-to-rim graben widths). Model results show that a 1-km-thick cooling unit can form within a crater if successive several-hundred-meter-thick flows occur within ~ 1000 years of each other. A lack of comparably thick cooling units on the Moon may account for the absence of similar patterns of graben in lunar mare basins.

[52] Consistent with observational constraints, the widest graben are predicted to occur in craters where pooled lavas were thickest, and no graben are predicted in plains exterior to craters and basins in settings where lavas did not pool and cooling units were thin. This scenario is consistent with plains formation on Mercury by the eruption of voluminous, low-viscosity flows, analogous to flood volcanic deposits on Earth [Head *et al.*, 2011]. Thermal contraction as an explanation for the formation of graben within the northern plains is consistent with the observation that most of the graben-hosting impact features were basins rather than smaller craters, as the former were sufficiently deep to capture substantial thicknesses of pooled lava but were not so deeply buried as to be no longer discernible. This scenario is also consistent with a tendency for the graben-hosting impact features to be located near the center of the northern plains where flow thicknesses would be expected to be greatest. The special combination of high-volume, low-viscosity flows and cooling of thick lava deposits in impact basins, and particularly their interior craters, accounts for a range of characteristics of tectonic landforms on Mercury that are not seen elsewhere in the solar system.

[53] **Acknowledgments.** The MESSENGER project is supported by the NASA Discovery Program under contracts NASW-00002 to the Carnegie Institution of Washington and NAS5-97271 to The Johns Hopkins University Applied Physics Laboratory. This work was also supported by NASA grant PGG09-0053 (AMF).

References

- Ahrens, T. J., K. Xia, and D. Coker (2001), Depth of cracking beneath impact craters: New constraint for impact velocity, in *Shock Compression of Condensed Matter-2001*, edited by M. D. Furnish, N. N. Thadhani, and Y. Horie, *AIP Conf. Proc.*, 620, 1393–1396.
- Anderson, E. M. (1951), *The Dynamics of Faulting*, 206 pp., Oliver and Boyd, Edinburgh, U. K.
- Arndt, N. (2008), *Komatiite*, 467 pp., Cambridge Univ. Press, New York, doi:10.1017/CBO9780511535550.
- Baker, D. M. H., J. W. Head, S. C. Schon, C. M. Ernst, L. M. Prockter, S. L. Murchie, B. W. Denevi, S. C. Solomon, and R. G. Strom (2011), The transition from complex crater to peak-ring basin on Mercury: New observations from MESSENGER flyby data and constraints on basin formation models, *Planet. Space Sci.*, 59, 1932–1948, doi:10.1016/j.pss.2011.05.010.
- Barnouin, O. S., M. T. Zuber, D. E. Smith, G. A. Neumann, R. R. Herrick, J. E. Chappelou, S. L. Murchie, and L. M. Prockter (2012), The morphology of craters on Mercury: Results from the MESSENGER flybys, *Icarus*, 219, 414–427, doi:10.1016/j.icarus.2012.02.029.
- Coffin, M. F., and O. Eldholm (1993), Scratching the surface: Estimating dimensions of large igneous provinces, *Geology*, 21, 515–518, doi:10.1130/0091-7613(1993)021<0515:STSEDO>2.3.CO;2.
- Denevi, B. W., et al. (2009), The evolution of Mercury's crust: A global perspective from MESSENGER, *Science*, 324, 613–618.
- Dombard, A. J., and S. A. Hauck (2008), Despinning plus global contraction and the orientation of lobate scarps on Mercury: Predictions for MESSENGER, *Icarus*, 198, 274–276, doi:10.1016/j.icarus.2008.06.008.
- Fassett, C. I., J. W. Head, D. T. Blewett, C. R. Chapman, J. L. Dickinson, S. L. Murchie, S. C. Solomon, and T. R. Watters (2009), Caloris impact basin: Exterior geomorphology, stratigraphy, morphometry, radial sculpture, and smooth plains deposits, *Earth Planet. Sci. Lett.*, 285, 297–308, doi:10.1016/j.epsl.2009.05.022.
- Freed, A. M., H. J. Melosh, and S. C. Solomon (2001), Tectonics of mascon loading: Resolution of the strike-slip faulting paradox, *J. Geophys. Res.*, 106, 20,603–20,620, doi:10.1029/2000JE001347.
- Freed, A. M., S. C. Solomon, T. R. Watters, R. J. Phillips, and M. T. Zuber (2009), Could Pantheon Fossae be the result of the Apollodorus crater-forming impact within the Caloris basin, Mercury?, *Earth Planet. Sci. Lett.*, 285, 320–327, doi:10.1016/j.epsl.2009.02.038.
- Freed, A. M., T. Herring, and R. Bürgmann (2010), Steady-state laboratory flow laws alone fail to explain postseismic observations, *Earth Planet. Sci. Lett.*, 300, 1–10, doi:10.1016/j.epsl.2010.10.005.
- Hauck, S. A., II, A. J. Dombard, R. J. Phillips, and S. C. Solomon (2004), Internal and tectonic evolution of Mercury, *Earth Planet. Sci. Lett.*, 222, 713–728, doi:10.1016/j.epsl.2004.03.037.
- Head, J. W., et al. (2011), Flood volcanism in the northern high latitudes of Mercury revealed by MESSENGER, *Science*, 333, 1853–1856, doi:10.1126/science.1211997.
- Hiesinger, H., J. W. Head III, U. Wolf, R. Jaumann, and G. Neukum (2011), Ages and stratigraphy of lunar mare basalts: A synthesis, in *Recent Advances and Current Research Issues in Lunar Stratigraphy*, edited by W. A. Ambrose and D. A. Williams, *Spec. Pap. Geol. Soc. Am.*, 477, 1–51.
- Hirth, G. (2002), Laboratory constraints on the rheology of the upper mantle, *Rev. Mineral. Geochem.*, 51, 97–120, doi:10.2138/gsrmg.51.1.97.
- Kennedy, P. J., A. M. Freed, and S. C. Solomon (2008), Mechanics of faulting in and around Caloris basin, Mercury, *J. Geophys. Res.*, 113, E08004, doi:10.1029/2007JE002992.
- Klimczak, C., T. R. Watters, C. M. Ernst, A. M. Freed, P. K. Byrne, S. C. Solomon, D. M. Blair, and J. W. Head (2012), Deformation associated with ghost craters and basins in volcanic smooth plains on Mercury: Strain analysis and implications for plains evolution, *J. Geophys. Res.*, 117, E00L03, doi:10.1029/2012JE004100.
- Matsuyama, I., and F. Nimmo (2009), Gravity and tectonic patterns of Mercury: Effect of tidal deformation, spin-orbit resonance, nonzero eccentricity, despinning, and reorientation, *J. Geophys. Res.*, 114, E01010, doi:10.1029/2008JE003252.
- Melosh, H. J. (1978), The tectonics of mascon loading, *Proc. Lunar Planet. Sci. Conf.*, 9th, 3513–3525.
- Melosh, H. J., and D. Dzursin (1978), Tectonic implications for gravity structure of Caloris basin, Mercury, *Icarus*, 33, 141–144, doi:10.1016/0019-1035(78)90029-5.
- Melosh, H. J., and W. B. McKinnon (1988), The tectonics of Mercury, in *Mercury*, edited by F. Vilas, C. R. Chapman, and M. S. Matthews, pp. 374–400, Univ. of Ariz. Press, Tucson.
- Melosh, H. J., and C. A. Williams (1989), Mechanics of graben formation in crustal rocks: A finite element analysis, *J. Geophys. Res.*, 94, 13,961–13,973, doi:10.1029/JB094iB10p13961.
- Mest, S. C. (2011), The geology of Schrödinger basin: Insights from post-Lunar Orbiter data, in *Recent Advances and Current Research Issues in Lunar Stratigraphy*, edited by W. A. Ambrose and D. A. Williams, *Spec. Pap. Geol. Soc. Am.*, 477, 95–115.
- Namiki, N., et al. (2009), Farside gravity field of the Moon from four-way Doppler measurements of SELENE (Kaguya), *Science*, 323, 900–905, doi:10.1126/science.1168029.
- Neumann, G. A., M. T. Zuber, D. E. Smith, and F. G. Lemoine (1996), The lunar crust: Global structure and signature of major basins, *J. Geophys. Res.*, 101, 16,841–16,843, doi:10.1029/96JE01246.
- Nittler, L. R., et al. (2011), The major-element composition of Mercury's surface from MESSENGER X-ray spectrometry, *Science*, 333, 1847–1850, doi:10.1126/science.1211567.
- Pike, R. J. (1988), Geomorphology of impact craters on Mercury, in *Mercury*, edited by F. Vilas, C. R. Chapman, and M. S. Matthews, pp. 165–273, Univ. of Ariz. Press, Tucson.
- Schultz, R. A., J. M. Moore, E. B. Grosfils, K. L. Tanaka, and D. Mége (2007), The Canyonlands model for planetary grabens: Revised physical basis and implications, in *The Geology of Mars: Evidence from Earth-Based Analogs*, edited by M. Chapman, pp. 371–379, Cambridge Univ. Press, New York, doi:10.1017/CBO9780511536014.016.

- Shoemaker, E. M., M. S. Robinson, and E. M. Eliason (1994), The south pole region of the Moon as seen by Clementine, *Science*, 266, 1851–1854, doi:10.1126/science.266.5192.1851.
- Smith, D. E., et al. (2012), Gravity field and internal structure of Mercury from MESSENGER, *Science*, 336, 214–217, doi:10.1126/science.1218809.
- Solomon, S. C. (1977), The relationship between crustal tectonics and internal evolution in the Moon and Mercury, *Phys. Earth Planet. Inter.*, 15, 135–145, doi:10.1016/0031-9201(77)90026-7.
- Solomon, S. C. (1978), On volcanism and thermal tectonics on one-plate planets, *Geophys. Res. Lett.*, 5, 461–464, doi:10.1029/GL005i006p00461.
- Solomon, S. C., and J. W. Head (1980), Lunar mascon basins: Lava filling, tectonics, and evolution of the lithosphere, *Rev. Geophys.*, 18, 107–141, doi:10.1029/RG018i001p00107.
- Strom, R. G., N. J. Trask, and J. E. Guest (1975), Tectonism and volcanism on Mercury, *J. Geophys. Res.*, 80, 2478–2507, doi:10.1029/JB080i017p02478.
- Thordarson, T., and S. Self (1998), The Roza Member, Columbia River Basalt Group: A gigantic pahoehoe lava flow field formed by endogenous processes?, *J. Geophys. Res.*, 103, 27,411–27,445, doi:10.1029/98JB01355.
- Vasavada, A. R., D. A. Paige, and S. E. Wood (1999), Near-surface temperatures on Mercury and the Moon and the stability of polar ice deposits, *Icarus*, 141, 179–193, doi:10.1006/icar.1999.6175.
- Watters, T. R., M. S. Robinson, and A. C. Cook (1998), Topography of lobate scarps on Mercury: New constraints on the planet's contraction, *Geology*, 26, 991–994, doi:10.1130/0091-7613(1998)026<0991:TOLSOM>2.3.CO;2.
- Watters, T. R., R. A. Schultz, M. S. Robinson, and A. C. Cook (2002), The mechanical and thermal structure of Mercury's early lithosphere, *Geophys. Res. Lett.*, 29(11), 1542, doi:10.1029/2001GL014308.
- Watters, T. R., M. S. Robinson, C. R. Bina, and P. D. Spudis (2004), Thrust faults and the global contraction of Mercury, *Geophys. Res. Lett.*, 31, L04701, doi:10.1029/2003GL019171.
- Watters, T. R., F. Nimmo, and M. S. Robinson (2005), Extensional troughs in the Caloris basin of Mercury: Evidence of lateral crustal flow, *Geology*, 33, 669–672, doi:10.1130/G21678.1.
- Watters, T. R., S. C. Solomon, M. S. Robinson, J. W. Head, S. L. André, S. A. Hauck, and S. L. Murchie (2009), The tectonics of Mercury: The view after MESSENGER's first flyby, *Earth Planet. Sci. Lett.*, 285, 283–296, doi:10.1016/j.epsl.2009.01.025.
- Watters, T. R., S. C. Solomon, C. Klimczak, A. M. Freed, J. W. Head, C. M. Ernst, D. M. Blair, T. A. Goudge, and K. P. Byrne (2012), Extension and contraction within volcanically buried impact craters and basins on Mercury, *Geology*, doi:10.1130/G33725.1, in press.
- Weider, S. Z., L. R. Nittler, R. D. Starr, T. J. McCoy, K. R. Stockstill-Cahill, P. K. Byrne, B. W. Denevi, J. W. Head, and S. C. Solomon (2012), Chemical heterogeneity on Mercury's surface revealed by the MESSENGER X-Ray Spectrometer, *J. Geophys. Res.*, 117, E00L05, doi:10.1029/2012JE004153.
- Zhong, S. (1997), Dynamics of crustal compensation and its influences on crustal isostasy, *J. Geophys. Res.*, 102, 15,287–15,299, doi:10.1029/97JB00956.
- Zuber, M. T., et al. (2010), Accommodation of lithospheric shortening on Mercury from altimetric profiles of ridges and lobate scarps measured during MESSENGER flybys 1 and 2, *Icarus*, 209, 247–255, doi:10.1016/j.icarus.2010.02.026.
- Zuber, M. T., et al. (2012), Topography of the northern hemisphere of Mercury from MESSENGER laser altimetry, *Science*, 336, 217–220, doi:10.1126/science.1218805.